



## Article

# Monitoring Mining Activities Using Sentinel-1A InSAR Coherence in Open-Pit Coal Mines

Lili Wang<sup>1,2</sup> , Liao Yang<sup>1,\*</sup>, Weisheng Wang<sup>1</sup>, Baili Chen<sup>1,2</sup> and Xiaolin Sun<sup>1,2</sup>

- <sup>1</sup> State Key Laboratory of Desert and Oasis Ecology, Xinjiang Institute of Ecology and Geography, Chinese Academy of Sciences, Urumqi 830011, China; wanglili19@mails.ucas.ac.cn (L.W.); wangws@ms.xjb.ac.cn (W.W.); chenbaili19@mails.ucas.ac.cn (B.C.); sunxiaolin19@mails.ucas.ac.cn (X.S.)
- <sup>2</sup> College of Resources and Environment, University of Chinese Academy of Sciences, Beijing 100049, China
- \* Correspondence: yangliao@ms.xjb.ac.cn

**Abstract:** Long-term continuous monitoring of the mining activities in open-pit coal mines is conducive to planning and management of the mining operations. Additionally, this facilitates assessment on their environmental impact and supervises illegal mining behaviors. Interferometric Synthetic Aperture Radar (InSAR) technology can be effectively applied in the monitoring of open-pit mines where vegetation is sparse and land cover is dominated by bare rock. The main objective of this study is to monitor the mining activities of four open-pit coal mines in the Wucaiwan mining area in China from 2018 to 2020, namely No. 1, No. 2 (containing two mining areas), and No. 3. We use the normalized differential activity index (NDAI) based on the coherence coefficient as an indicator of the mine activity due to its robustness to temporal and spatial decorrelation. After analyzing and removing the decorrelation caused by rain and snow weather, 70 NDAI images in 12-day intervals are obtained from Sentinel-1A InSAR coherence images. Then, the annually-averaged NDAI images are applied to an RGB composite technique (red for 2018, green for 2019, blue for 2020) to express the interannual variation of the mining activities. Points of interest are then selected for NDAI time series analysis. The RGB composite results indicated that No. 1 and 3 open-pit coal mines were continuously mined during the three years; whereas, the two mining areas of No. 2 were mainly active in 2018. The 12-day NDAI time-series graphs of No. 2 open-pit coal mine also indicate that the coal piles located in the coal transferring area of the first mining area were not completely removed until April 2019. It is also seen that the second mining area was decommissioned in November 2018 and became rehabilitated in July 2019. Results were validated using the Sentinel-2A images and related background information confirming the efficiency of the proposed approach for monitoring the mining activity in open-pit mines.

**Keywords:** Sentinel-1A; InSAR coherence; open-pit coal mine; mining activity; NDAI



**Citation:** Wang, L.; Yang, L.; Wang, W.; Chen, B.; Sun, X. Monitoring Mining Activities Using Sentinel-1A InSAR Coherence in Open-Pit Coal Mines. *Remote Sens.* **2021**, *13*, 4485. <https://doi.org/10.3390/rs13214485>

Academic Editors: Denis Guilhot, Radosław Zimroz, Fabio Remondino and Vittorio Cannas

Received: 11 October 2021  
Accepted: 5 November 2021  
Published: 8 November 2021

**Publisher's Note:** MDPI stays neutral with regard to jurisdictional claims in published maps and institutional affiliations.



**Copyright:** © 2021 by the authors. Licensee MDPI, Basel, Switzerland. This article is an open access article distributed under the terms and conditions of the Creative Commons Attribution (CC BY) license (<https://creativecommons.org/licenses/by/4.0/>).

## 1. Introduction

Open-pit coal mining activity often causes large-scale and high-intensity ecological disturbances, resulting in substantial impacts such as surface damage, air pollution, soil erosion, and degradation of ecosystem functions [1]. Open-pit coal mining is the dominant production method in the Wucaiwan mine located in the western part of the Zhundong coalfield at Xinjiang, China. Since the development of this coalfield in 2006, coal mining and coal-chemical industry have significantly affected the surrounding ecological environment [2]. Furthermore, the increasing number of mining faces in the Wucaiwan mine area raises concerns regarding cross-border and unlicensed mining activities [3]. Illegal mining can cause extra environmental issue as they often ignore regulated mining methods [4]. Therefore, continuous monitoring of open-pit coal mining activities is an utmost necessity and enables efficient planning and managing of mining operations by accessing their impact on the environment and enforcing relevant regulations.

Remote sensing is widely used to monitor open-pit mines due to its versatile spatial and temporal characteristics. For instance, unmanned aerial vehicles (UAVs) mapping technology is used to construct three-dimensional (3D) models of open-pit mines, map the environmental indicators, and monitor slope instability (see, e.g., Tong et al. [5]; Chen et al. [6]; Gong et al. [7]). High-resolution optical imagery has also been used to monitor land use and land cover (LULC) around open-pit mines and assess the impact of mining activities on the environment. (Nascimento et al. [8]; Asner et al. [9]; Wu et al. [10]). Nevertheless, the limitations of UAV's flight range make multiple flight sessions necessary to carry out monitoring of a large-area [5], which is undoubtedly a challenge for areas that cannot be continuously powered [11]. Optical images are also susceptible to weather conditions and are insensitive to vertical changes on the surface, making it more difficult to achieve continuous monitoring.

An alternative to UAVs and optical satellite imaging is synthetic aperture radar (SAR) imaging which provides many advantages including the capability to work in all weather, all day, and over wide coverage. Hence, Interferometric Synthetic Aperture Radar (InSAR) technology based on SAR data is equipped with capabilities to address a wide range, long time, and continuous ground monitoring. InSAR has been also used in other monitoring applications, such as tracking earthquakes [12], volcanic eruptions [13], ground stability at geoenery sites [14], landslides [15], glacier motion [16], land deformation [17], and underground mining-induced subsidence [18].

Currently, InSAR monitoring of open-pit mines also involves multiple aspects, including slope stability detection, illegal mining tracking, environmental impact assessment, and environmental indicators mapping. Paradella et al. [19] used integrated SAR analysis based on TerraSAR-X data to monitor ground instabilities in open-pit iron mines in Carajás Province. Hartwig et al. [20] also used the persistent scatterer interferometry (PSI) technique to monitor the deformation of mine slope to determine its risk. Wang et al. [21] also successfully determined the legal and illegal mining sites by using the decorrelation phenomenon of coherence images which provides a new monitoring method for illegal mining. Chaussard et al. [22] used InSAR techniques to determine that land subsidence around twenty black sand mining sites on Luzon Island had seriously threatened coastal towns. Chatterjee et al. [23] used InSAR coherence and DEM to successfully distinguish active, unreclaimed, and abandoned or closed open-pit mines, delineate overburden and coal dumps from the surrounding area.

Nevertheless, when using InSAR technology, it is still difficult to quantitatively analyze the mining activities by surface subsidence inside the pit. This is because the short-term drastic changes in the surface topography result in substantial decorrelation [24]. As a response to this defect, in this study, we transform the decorrelation problem into available information to monitor the mining activities of the Wucaiwan open-pit mine from 2018 to 2020. We first analyze the temporal and spatial decorrelation contained in the stable points extracted based on the time-averaged ( $>0.9$ ) and standard deviation ( $<0.1$ ) of coherence images. We then eliminate the decorrelation caused by bad weather. The decorrelation noise, which is not related to the distributed scatterers, is then removed using the normalized difference activity index (NDAI) with the stable points as a reference. The NDAI is robust against temporal and spatial decorrelation noise and is commonly used as an activity indicator to express mining activities. The NDAIs are averaged to observe the overall mining activities from 2018 to 2020. To represent an interannual variation of mining activity, we then use the RGB composite technique based on annually-averaged NDAI. Points of interest are selected to make NDAI time series graphs to determine the time of specific activities. To validate the proposed method and examine its efficiency, the results are also compared with the Sentinel-2A images and related background information [25–27] of the Wucaiwan open-pit mine.

## 2. Materials

### 2.1. Study Area

The Wucaiwan open-pit mine is located in Jimsar County, Xinjiang Changji Hui Autonomous Prefecture in northwestern China (Figure 1). The open-pit mine spans 36.39 km from east to west and 38.75 km from north to south. The proven coal reserves include about 30.803 billion tons, accounting for about 1% of the national coal reserves. It began operating in 2006 and now contains five open-pit coal mines [28,29]. In this study, only No. 1, 2, and 3 open-pit coal mines are studied as No. 4 and No. 5 have not been completely developed [26].

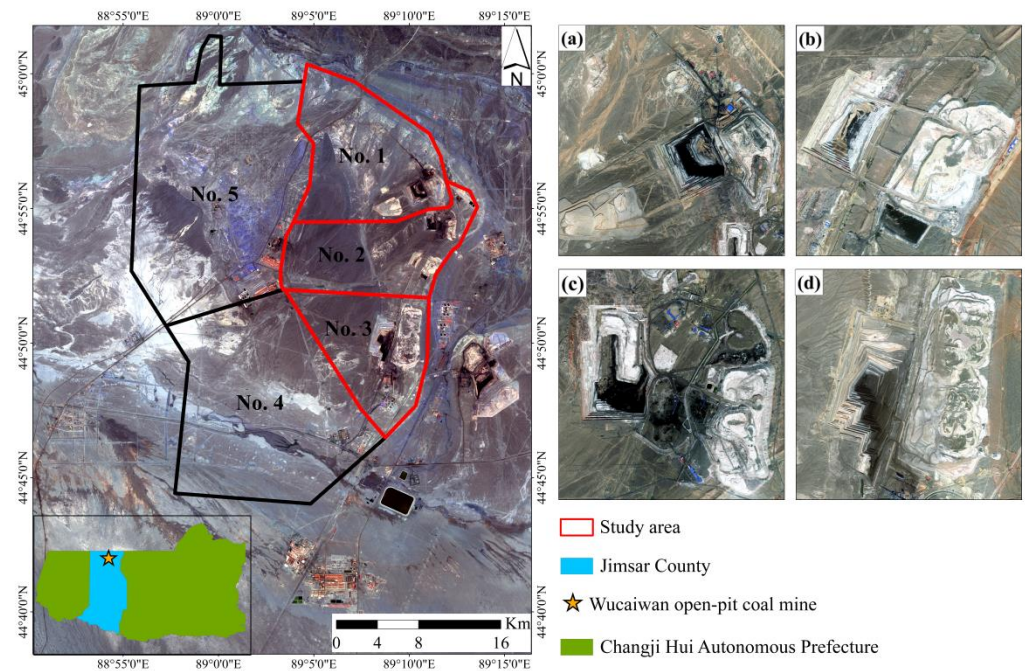


**Figure 1.** Location of Wucaiwan open-pit mine in China. The four right optical images are from Google Earth: (a) No. 1 open-pit coal mine; (b) first mining area of No. 2 open-pit coal mine; (c) the second mining area of No. 2 open-pit coal mine, and (d) No. 3 open-pit coal mine.

No. 1 open-pit coal mine (Figure 1a) started production in 2009 and currently covers approximately 50.87 km<sup>2</sup>, with a construction scale of 7 Mt/a [25]. No. 2 open-pit coal mine contains two mining areas, the first mining area (Figure 1b) is in the south and the second mining area (Figure 1c) is in the north. The mines started production in 2009 with a construction scale of 4 Mt/a [26]. No. 3 open-pit coal mine (Figure 1d) was the first mine that started producing coal in 2007 and had the largest annual coal output about 20 Mt/a [27].

The study area has low rainfall, sparse vegetation, and a predominantly bare rock land cover. It is suitable for interferometric processing using Sentinel-1A C-band data for long-term monitoring of open-pit coal operations.

### 2.2. Dataset

#### 2.2.1. Sentinel-1A SAR Data

Sentinel-1A is an earth observation satellite carrying the C-band synthetic aperture radar instruments that were launched by European Space Agency (ESA) on 3 April 2014. This satellite has a 12-day revisit period and makes observations day and night in all weather conditions. Sentinel-1A uses a new form of ScanSAR imaging known as Terrain Observation with Progressive Scans SAR (TOPSAR) [30]. It has the same resolution (about 4 m in range and 14 m in azimuth) as ScanSAR but with a higher signal-to-noise ratio [31]. Sentinel-1A operates in four particular imaging modes with different resolutions and

coverages including Stripmap (SM), Interferometric Wide Swath (IW), Extra Wide Swath (EW), and Wave (WV) [32]. The IW mode is commonly used in various studies. The instrument that operates the IW imaging mode supports dual-polarization (HH+HV, VV+VH) [32]. In this study, 92 Sentinel-1A IW mode Single Look Complex (SLC) SAR images are considered to detect mining activities in the Wucaiwan open-pit mine. These images were captured between 3 January 2018 and 30 December 2020 in ascending track. All Sentinel-1A images were downloaded from Alaska Satellite Facility (ASF) [33]. The detailed information of the acquired Sentinel-1A SAR images is also presented in Table 1.

**Table 1.** Detailed information of Sentinel-1A SAR images used in this study.

Parameter	Value
Wavelength	5.6 cm
Frequency	5.405 GHz
Polarization	VV
Product Type	Level-1 SLC
Revisit period	12 days
Incidence angle	38.98°
Pixel spacing in slant range	2.33 m
Pixel spacing in azimuth	13.91 m
Pass direction	Ascending
Acquisition date	3 January 2018 through 30 December 2020

### 2.2.2. Sentinel-2A Optical Data

Sentinel-2A is a satellite equipped with multispectral instruments that was launched by ESA on 23rd of June 2015. This satellite has 13 spectral bands with different spatial resolutions, including three visible and near-infrared bands in 10 m, four red edge and two shortwave infrared bands in 20 m, three atmospheric correction bands in 60 m, and a ten-day revisit cycle [34]. In this study, three cloud-free L2A-level Sentinel-2A multispectral images are collected for validation. The images were captured on 4 August 2018, 21 May 2019, and 9 June 2020, respectively. They are used as the reference data to verify the annual mining activities of open-pit coal mines monitored by SAR data. Amongst the 13 spectral bands, the red, green, and blue bands with a resolution of 10 m are the most suitable for feature identification [35]. The Sentinel-2A optical images were freely acquired from the Copernicus Data Center (CDC) [36].

### 2.2.3. DEM

In InSAR processing, a digital elevation model (DEM) is introduced to simulate and remove the topographic phase component from the interferograms. Although the topography of the active open-pit mines is constantly changing, the short perpendicular baseline of Sentinel-1A is hardly affected by the DEM errors [37]. Hence, the conventional SRTM DEM is sufficient to remove the topographic phase. The SRTM is a 30 m resolution DEM produced by the National Aeronautics and Space Administration (NASA) and National Geospatial-Intelligence Agency (NGA) in 2000 for the Endeavour space shuttle carrying a C-band sensor via InSAR processing. The SRTM data were also acquired from the United States Geological Survey (USGS) [38].

## 3. Methods

### 3.1. Generation of Coherence Images

The coherence image is one of the interferometric products generated by the InSAR processing of two SAR images. The two images are captured from the same area acquired in repeat pass orbits. The coherence values are used to express the similarity of radar reflection between two SAR images. If the reflective properties from the same target in both images are changed, the coherence values of that target are accordingly reduced which is also described as phase decorrelation.

The coherence values can be estimated using local coherence, that is the cross-correlation coefficient of the SAR image pair estimated over a small window [39,40]. The coherence,  $\gamma$ , between the two complex SAR images is calculated as:

$$\gamma = \frac{\left| \sum_{i=1}^L \sum_{j=1}^N M(x_i, z_j) S^*(x_i, z_j) \right|}{\sqrt{\sum_{i=1}^L \sum_{j=1}^N |M(x_i, z_j)|^2 \sum_{i=1}^L \sum_{j=1}^N |S(x_i, z_j)|^2}} \quad (1)$$

where  $M$  and  $S$  are the complex pixel values of the two SAR images. The coherence value of a pixel is estimated using the kernels with  $L \times M$  pixels and its value is between 0 and 1, where 0 and 1 denote complete decorrelation and the absence of noise, respectively. As a statistical value, the coherence value cannot quantitatively measure the ground scatterers' disturbances; however, it represents the fraction of power that is scattered by the unchanged parts of the scene [41].

In this paper, we use SNAP [42] software to perform interferometric processing on the 92 available SAR images with a 12-day temporal baseline and generate 91 coherence images. In the processing, all SAR images are cropped to reduce the processing time. Sentinel-1A precise orbit files are also downloaded by the apply-orbit-file tool to improve the geocoding and subsequent SAR processing results. The orbit file and external SRTM DEM data are introduced to coregister the master and slave images by the back-geocoding operator. The interferogram and coherence images are then generated by calculating the phase difference and cross-correlation coefficient in the interferogram step. The flat-earth and topographic phases are then removed using the SRTM DEM data. To reduce the speckle noise, Goldstein phase filtering is used for all coherence images. Finally, to superimpose the coherence and optical images for further analysis, the terrain correction is applied and orthorectified coherence images are generated. Figure 2 shows the entire workflow of the proposed method.

### 3.2. Extraction of the Stable Points

To obtain stable points within the study area, the average and standard deviation of 91 coherence images are calculated. The time-averaged coherence and standard deviation coherence maps are presented in Figure 3a,b. Stable points are also extracted based on pixels with time-averaged coherence values greater than 0.9 and standard deviations less than 0.1 (Figure 3c).

### 3.3. Normalized Difference Activity Index (NDAI)

In repeat-pass interferometry, the coherence decorrelation usually includes thermal, spatial, and temporal decorrelation [43–46]. Thermal noise is also generally ignored [47]. Spatial decorrelation (also known as “baseline decorrelation”) is further divided into volumetric decorrelation and surface decorrelation. Volumetric decorrelation usually occurs in the areas with high penetration such as forest canopies. The Wucaiwan open-pit mine is however located in an arid desert area, hence the volumetric decorrelation is directly excluded. Surface decorrelation is mainly caused by the local slope formed by the topographic relief. Although the short baseline and large range bandwidth of Sentinel-1A partly reduces the surface decorrelation, there is still surface decorrelation due to the complexity of the post-mining topography [48]. Temporal decorrelation is related to the changes in the dielectric and structural properties of the scatters [49]. Therefore, natural phenomena such as rain and snow, natural growth and leaves falling in the vegetated areas, and man-made activities cause the temporal decorrelation [50]. In the study area, the vegetation is sparse, and land cover is dominated by the bare rock; thus, the temporal decorrelation is mainly caused by mining activities and rain, snow, and other weather conditions.

Based on the above analysis, we focus on the coherence decorrelation defined as:

$$\gamma = \gamma_{\text{spatial}} \cdot \gamma_{\text{temporal}} = \gamma_{\text{surface}} \cdot \gamma_{\text{activity}} \cdot \gamma_{\text{weather}} \quad (2)$$

where  $\gamma_{\text{activity}}$  indicates the temporal decorrelation caused by coal mining,  $\gamma_{\text{weather}}$  is the temporal decorrelation due to snow and rain, and  $\gamma_{\text{surface}}$  indicates the spatial decorrelation caused by the perpendicular baseline between the two SAR images.

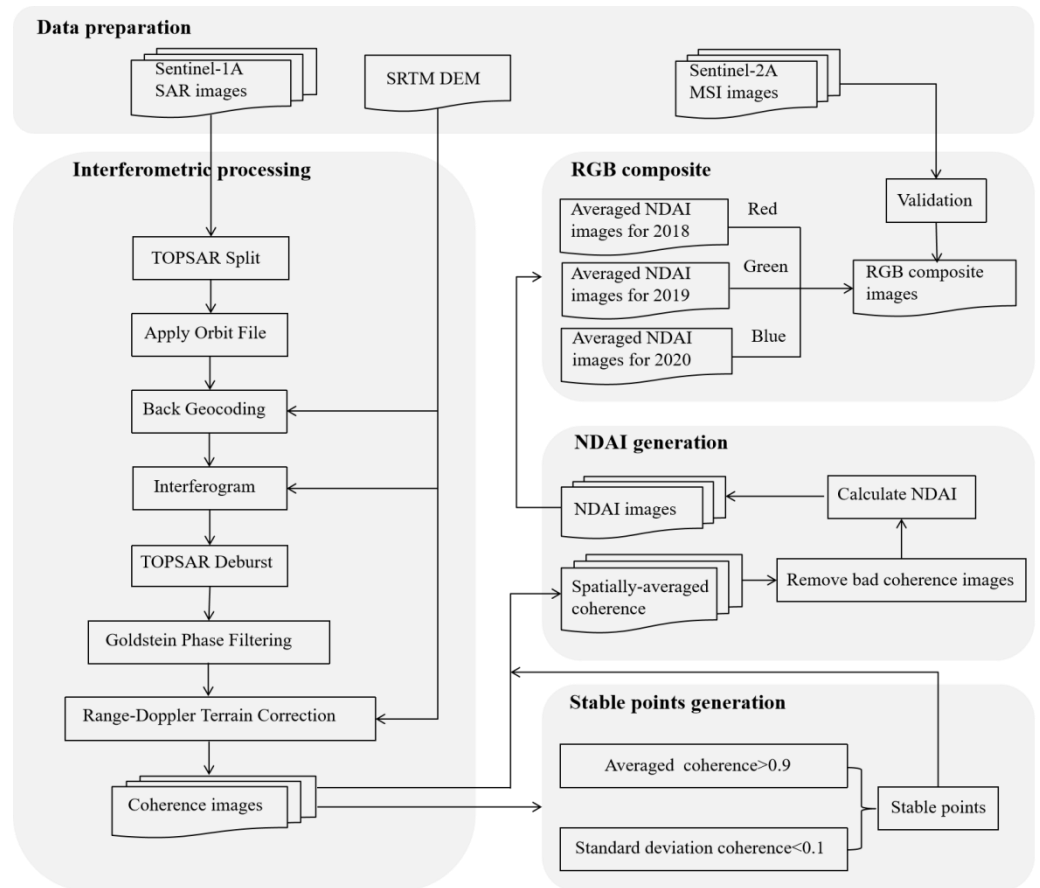


**Figure 2.** Workflow for monitoring open-pit mining activities by normalized difference activity index (NDAI) based on the InSAR coherence images. The process includes data preparation, interferometric processing, stable points analysis, NDAI calculation, and generating the RGB composite.

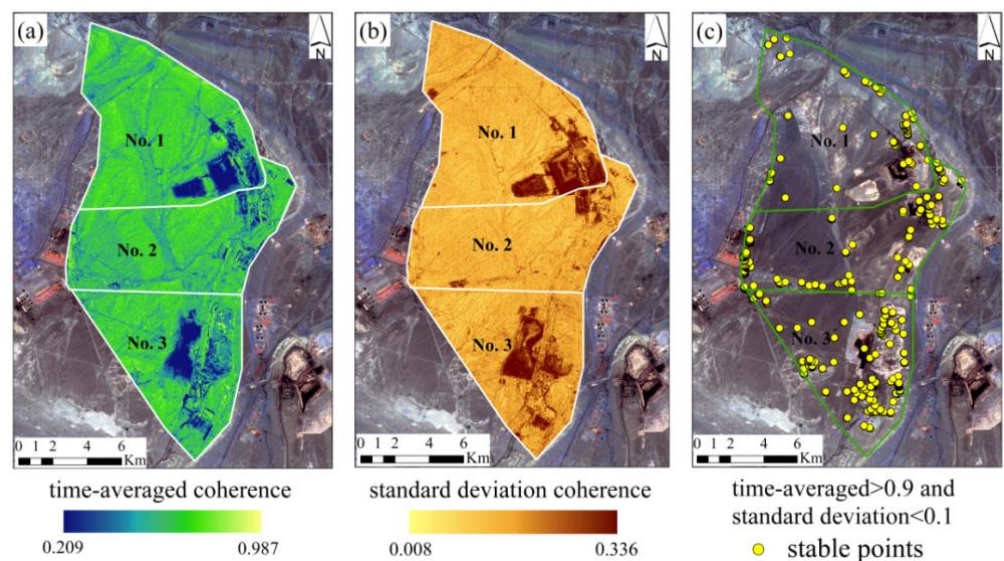


**Figure 3.** The process of selecting stable points: (a) time-averaged coherence map; (b) standard deviation coherence map, and (c) stable points map.

The main objective here is to remove  $\gamma_{\text{surface}}$  and  $\gamma_{\text{weather}}$  of the target areas and highlight  $\gamma_{\text{activity}}$  based on the stable points obtained from the time-averaged coherence and the standard deviation coherence maps. To analyze the weather-induced temporal decorrelation, we calculate the spatial mean of the stable points on each coherence image. It is seen that most of the coherence images with a spatial mean less than 0.9 are those from winter. We speculate that this is most likely a snow-induced decorrelation (see, Figure 4a). Therefore, we remove the weather-induced decorrelation  $\gamma_{\text{weather}}$  by excluding these coherence images which leaves us with 70 coherence images. The coherence decorrelation is therefore expressed as:

$$\gamma = \gamma_{\text{spatial}} \cdot \gamma_{\text{temporal}} = \gamma_{\text{surface}} \cdot \gamma_{\text{activity}} \quad (3)$$

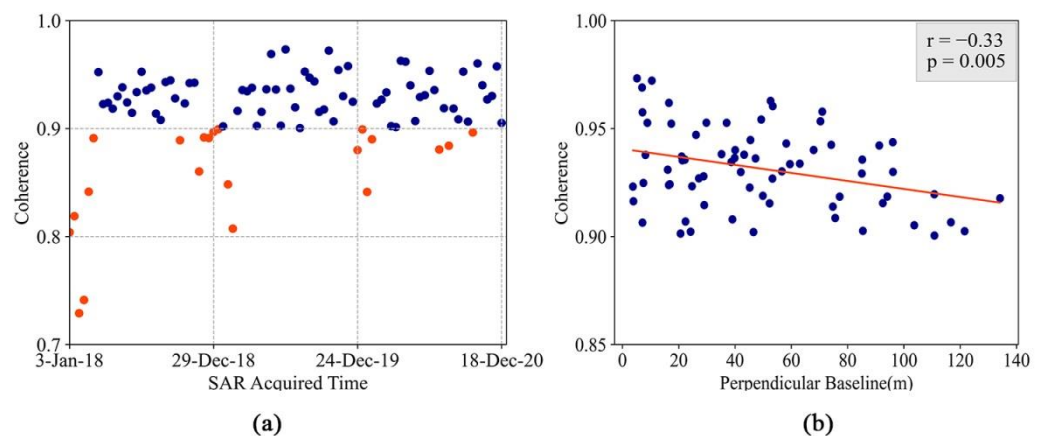


**Figure 4.** The process of analyzing decorrelation using the spatially averaged coherence values of stable points obtained based on coherence images with 12-day intervals: (a) The relationship between the spatially averaged coherence values of the stable points and the SAR images acquisition time as a function. Coherence images represented by yellow points are excluded from further analysis. (b) Pearson’s correlation coefficient and linear regression analysis of the relationship of the spatially averaged coherence values of the stable points and the absolute values of perpendicular baseline.

We then notice that although the Sentinel-1A data have a small orbit tube, it still affects the coherence value. Therefore, for the stable points in the remaining 70 coherence images, we need to measure the relationship between the absolute values of perpendicular baseline and the spatially averaged coherence values. Here, we perform linear regression and calculate Pearson’s correlation coefficient. A weak negative correlation is found by the correlation coefficient  $r$  which is equal to  $-0.33$  and  $p$ -value is less than  $0.05$  indicating that the correlation is significant (Figure 4b). This suggests that there still exists the surface decorrelation caused by the perpendicular baseline. To remove  $\gamma_{\text{surface}}$ , we introduce the normalized difference activity index (NDAI) proposed by Moon and Lee in 2021 [51].

The NDAI is defined as an index that reduces the noise signals based on stable points and indicates mining activity:

$$\text{NDAI} = \frac{\gamma_{\text{stable}}^{\text{stable}} - \gamma_{\text{target}}^{\text{target}}}{\gamma_{\text{stable}}^{\text{stable}} + \gamma_{\text{target}}^{\text{target}}} \quad (4)$$

where  $\gamma_{\text{stable}}^{\text{stable}}$  is the spatial mean of the stable points on each coherence image, and  $\gamma_{\text{target}}^{\text{target}}$  is the coherence values of the target region on each coherence image. Using Equations (3) and (4) we then write:

$$\text{NDAI} = \frac{\gamma_{\text{surface}}^{\text{stable}} \cdot \gamma_{\text{activity}}^{\text{stable}} - \gamma_{\text{surface}}^{\text{target}} \cdot \gamma_{\text{activity}}^{\text{target}}}{\gamma_{\text{surface}}^{\text{stable}} \cdot \gamma_{\text{activity}}^{\text{stable}} + \gamma_{\text{surface}}^{\text{target}} \cdot \gamma_{\text{activity}}^{\text{target}}} \quad (5)$$

We further note that the reflective properties of stable points and target region do not affect the surface decorrelation, and their related temporal decorrelation is also removed in the above research. Therefore,  $\gamma_{\text{surface}}^{\text{stable}} \approx \gamma_{\text{surface}}^{\text{target}}$ , and NDAI only represent the active state of the target region:

$$\text{NDAI} = \frac{\gamma_{\text{activity}}^{\text{stable}} - \gamma_{\text{activity}}^{\text{target}}}{\gamma_{\text{activity}}^{\text{stable}} + \gamma_{\text{activity}}^{\text{target}}} \quad (6)$$

As seen in Equation (6), the NDAI value theoretically falls between 0 and 1, with higher NDAI values indicating more mining activities. We however notice that there are negative NDAIs, which are caused by the coherence values of the man-made target points that are higher than the coherence values of the stable points. Therefore, we exclude these points from our analysis.

### 3.4. Change Detection Using RGB Composite

The RGB composite technique is applied to the annually-averaged NDVI to visualize the interannual variation of mining activities in the mine areas between 2018 and 2020. Figure 5 displays the RGB composite scheme and the meaning of each color. Each annually-averaged NDVI image corresponds to a color channel, i.e., 2018 for the red channel, 2019 for the green channel, and 2020 for the blue channel. Red, green and blue indicates the mining areas that were active only in 2018, 2019, and 2020, respectively. In this setting, cyan, magenta, and yellow represent the mining areas that were stable only in 2018, 2019, and 2020, respectively, but were active in the other two years. The white color also means that the mining areas had always been active, whereas the black color indicates that the mining areas had always been stable during the above three years.

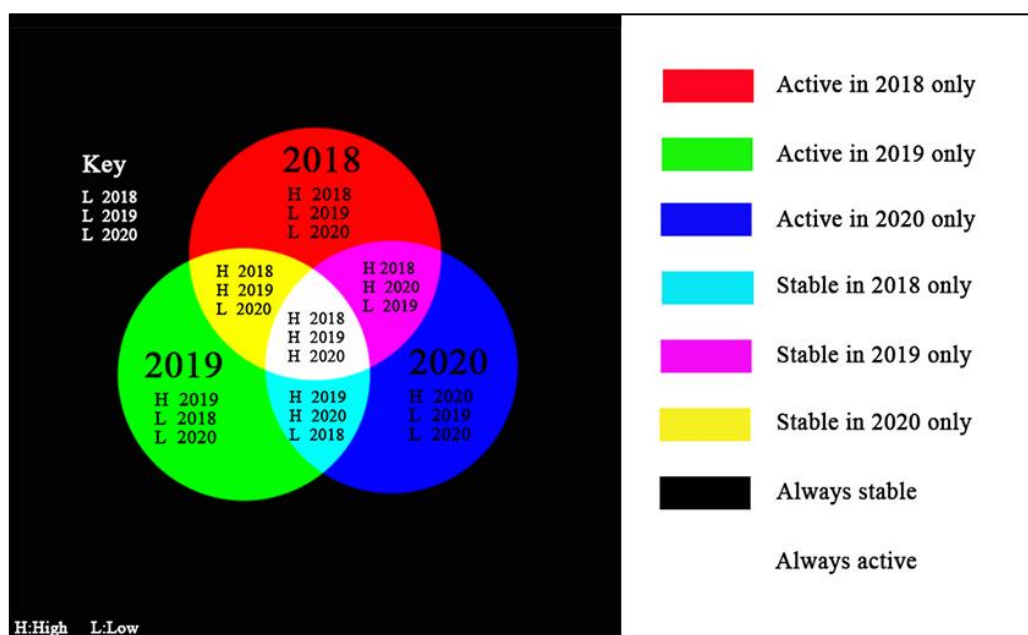


**Figure 5.** The left side of the figure is the RGB composite scheme based on annually-averaged NDAI images (red for 2018, green for 2019, blue for 2020). The RGB composite scheme is used in this study to represent the interannual variation of mining activity. The right side of the figure is the meaning of each color concerning the mining activity.

## 4. Results

### 4.1. Overall Change Detection Using Averaged NDAI Map

The overall mining activities of the Wucuiwan open-pit mine from 2018 to 2020 are examined by averaging 70 NDAI images obtained from the coherence images. The averaged NDAIs range between  $-0.03$  and  $0.66$ . The higher the averaged NDAIs the more intense

the mining activities. In this study, the NDAI values of greater than or equal to 0.2 are considered as active. We also combine the 2018 google earth image, 2020 Sentinel-2A MSI image, and Liu Xue's interpretation results of Landsat5, 7, 8, and GF1 images of Wucaiwan open-pit mine from 2007 to 2016 [3]. Based on that we then divide each open-pit coal mine area into three areas including coal mining, overburden dumping, and coal transferring areas.

As seen in Figure 6, due to the mining activities, the NDAI values of the open-pit coal mines are significantly higher than in other surrounding areas. Table 2 also presents the proportion of the pixels with  $NDAI \geq 0.2$  to the total pixels in each area in the coal mining areas, overburden dumping areas and coal transferring areas of No. 1, 2, and 3 open-pit coal mines. In terms of coal mining areas, the proportion of NDAIs greater than or equal to 0.2 in the mining areas of No. 1 and 3 open-pit coal mines are significantly higher than that of the No. 2 (No. 1: 90.3%, No. 2: 46.1%, No. 3: 76.3%). This indicates that No. 1 and 3 open-pit coal mines are more active and produced more coal than No. 2 during the three years.

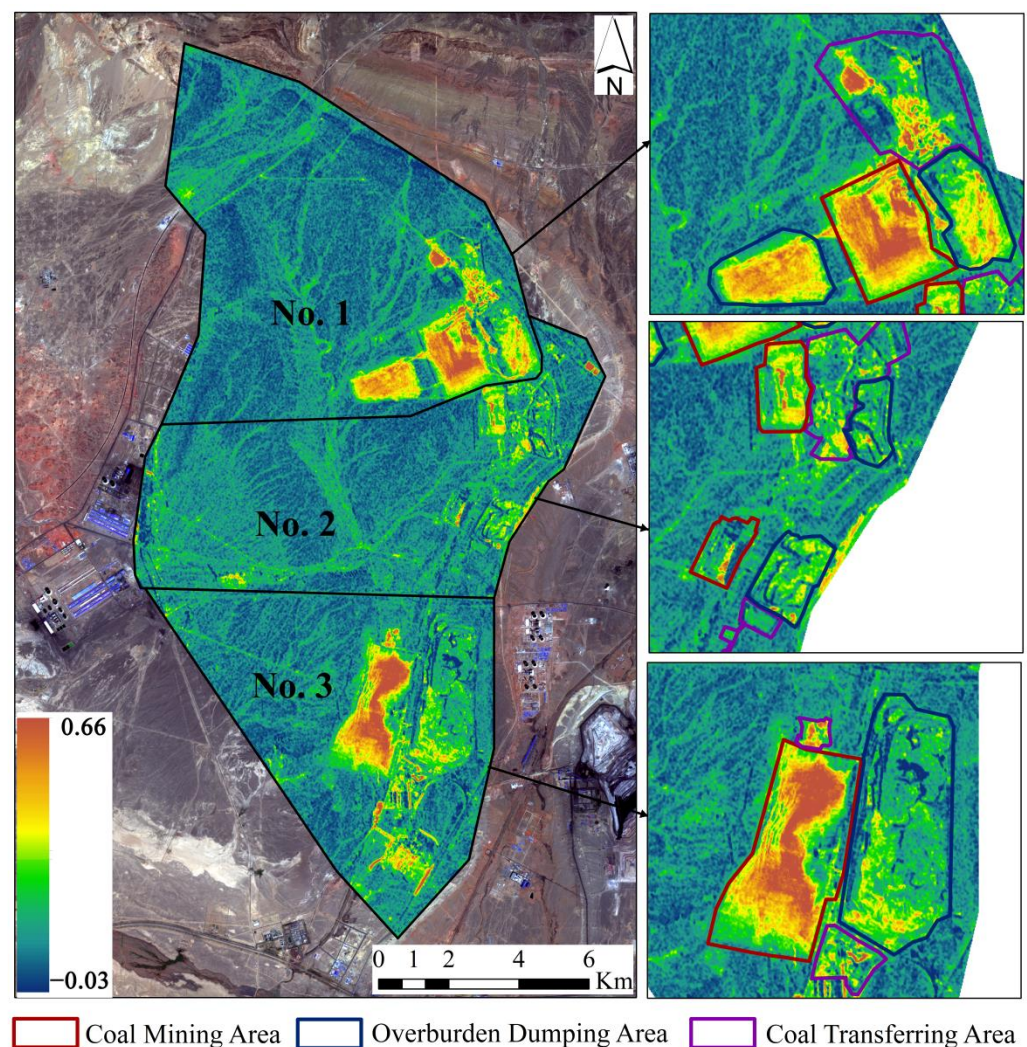


**Figure 6.** Overall mining activities map based on the averaged NDAI images over the Wucaiwan open-pit coal mine during 2018 to 2020. Brown areas correspond to high averaged NDAI values, whereas dark green areas have low averaged NDAI values. A higher NDAIs implies more intense mining activity.

**Table 2.** Percentage of the pixels with averaged NDAI  $\geq 0.2$  in each area.

	No. 1	No. 2	No. 3
Coal mining area	90.3%	46.1%	76.3%
Overburden dumping area	71.3%	34.2%	27.9%
Coal transferring area	32.6%	26.1%	55.6%

The overburden dumping area of the No. 1 open-pit coal mine is also covered by a large area of high NDAIs. This corresponds with the active state of the mining area (coal mining area: 90.3%, overburden dumping area: 71.3%). The overburden dumping area of No. 3 open-pit coal mine is exactly the opposite of the mining area, and the entire area has very few high NDAI values (coal mining area: 76.3%, overburden dumping area: 27.9%). This means that the No. 1 open-pit mine mainly adopts the mining method of overburden out-discharge, whereas the No. 3 open-pit mine is dominated by the mining method of overburden in-discharge. Using internal dumps can reduce land occupation, save costs, reduce the impact on the external environment, and restore the mining areas.

The coal transferring areas are used for handling and stockpiling coal include the buildings, haul trucks, and coal piles. Similar to the coal mining area, the coal transferring areas of No. 1 and 3 open-pit coal mines have more intense surface activity compared with No. 2 (No. 1: 32.6%, No. 2: 26.1%, No. 3: 55.6%), where in addition to the high NDAI values caused by changes in the coal piles there is also the possibility of demolition or new construction of buildings. Detailed mining activity information for each open-pit coal mine is presented in the next sections.

#### 4.2. Interannual Change Detection Using RGB Composite Map

Figure 7 shows the interannual variation of the Wucaiwan open-pit mine from 2018 to 2020 which is the RGB composite map of the three annually-averaged NDAI images (Red: 2018, Green: 2019, Blue: 2020). As it is seen there are large areas of white pixels in No. 1 and 3 open-pit coal mines. This suggests that these two mine areas had been continuously producing coal during the three years. Blue and cyan pixels are also widely distributed on the edges of both mining areas, indicating that the mining areas had been gradually expanded from 2019 to 2020. No. 2 open-pit coal mine has two mining areas, and the first mining area located in the south is covered by a large area of black pixels in the entire mining area. This also indicates that mining activities were stopped before 2018. However, the red pixels in the coal transferring area mean that this area has been active in 2018. The second mining area located in the north is mostly dominated by red pixels, representing that it may have been active in 2018 only and stable afterward. According to the “Xinjiang Tianlong Hope Energy Co., Ltd. Publicity of the Environmental Assessment Report of the Phase I Project of Wucaiwan No. 2 Open-pit Coal Mine” [26], the first mining area was forced to stop mining after November 2015 due to a lack of an environmental impact assessment (EIA) report. The second mining area also stopped mining in 2017 due to the expiry of the prospecting rights. In the following sub-sections, the mining activity from 2018 to 2020 for No. 1, 2, and 3 open-pit coal mines, respectively.

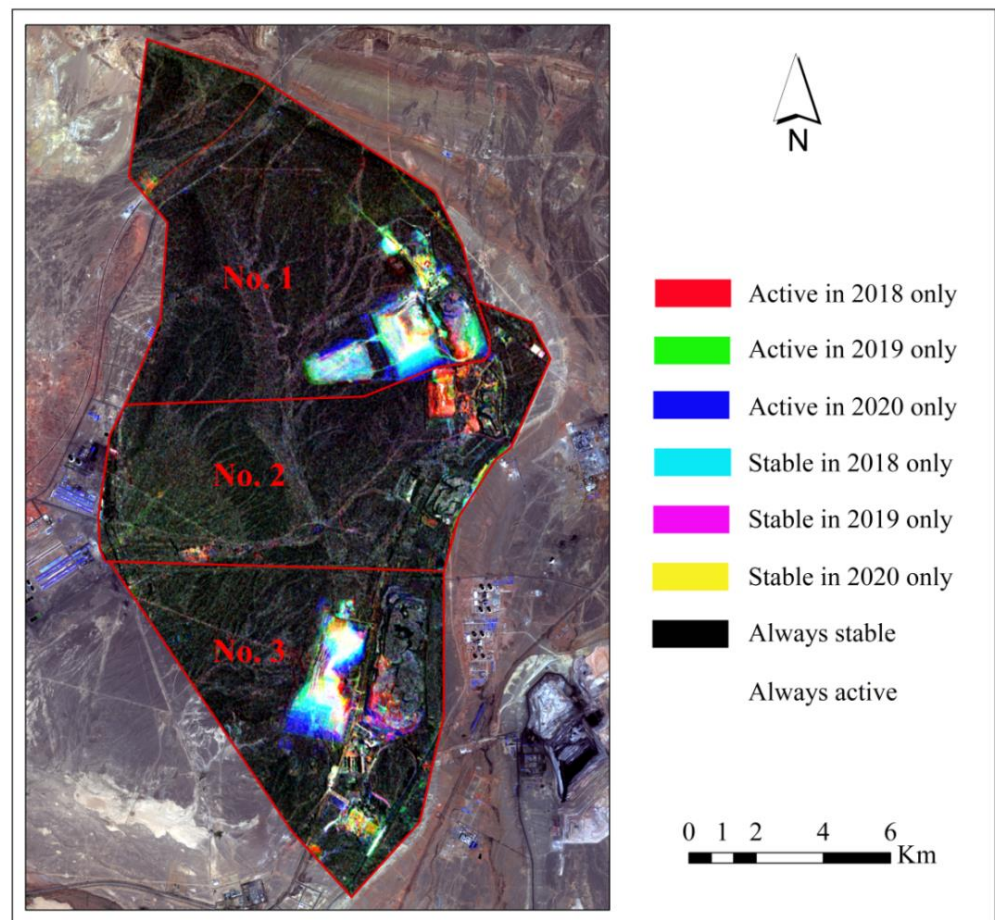


**Figure 7.** Interannual changes of mining activity map based on the RGB composite of the annually-averaged NDAI images where Red, Green, and Blue represent 2018, 2019, and 2020, respectively.

#### 4.2.1. No. 1 Open-Pit Coal Mine

The interannual variation of the mining activity map in No. 1 open-pit coal mine is shown in Figure 8. The cyan pixels distributed in the south of the coal mining area indicate that the surface of the area was covered by bare rock and unchanged in 2018. It became active sporadically or continuously in 2019 and 2020. It is also seen that the exploitation of the coal mining area has been moved towards the south direction. The result is the same as seen in the Sentinel-2A images (stable bare rock on 4 August 2018, open-pit mine bench on 21 May 2019, pit floor on 9 June 2020) (Figure 8a,d). The two overburden dumping areas located to the left and right of the mining area were both dumping and expanding between 2018 and 2020. The entire dumping area on the left is also dominated by white, green, and blue pixels. This indicates that the area was expanded westward in 2019 and northward in 2020 in addition to dumping during the three years. The Sentinel-2A images mainly represent the expansion of this dumping area to the north in 2020 (Figure 8a,e). The entire dumping area on the right is dominated by black, red, green, and blue pixels. The north side of the dumping area on the right is dominated by black pixels indicating no activity, while the south side is mainly covered by red, green, and blue pixels. The optical images also verify the area, where the red pixels were active only in 2018 (Figure 8a,c). The combination of optical images and RGB composite images further reveals that the surface changes in the coal transferring area are the results of the coal piles and buildings. For example, the expansion of a coal pile area in 2019 and 2020 can be observed through the RGB composite map (cyan pixels), which is the same as represented by the optical images (Figure 8a,b).

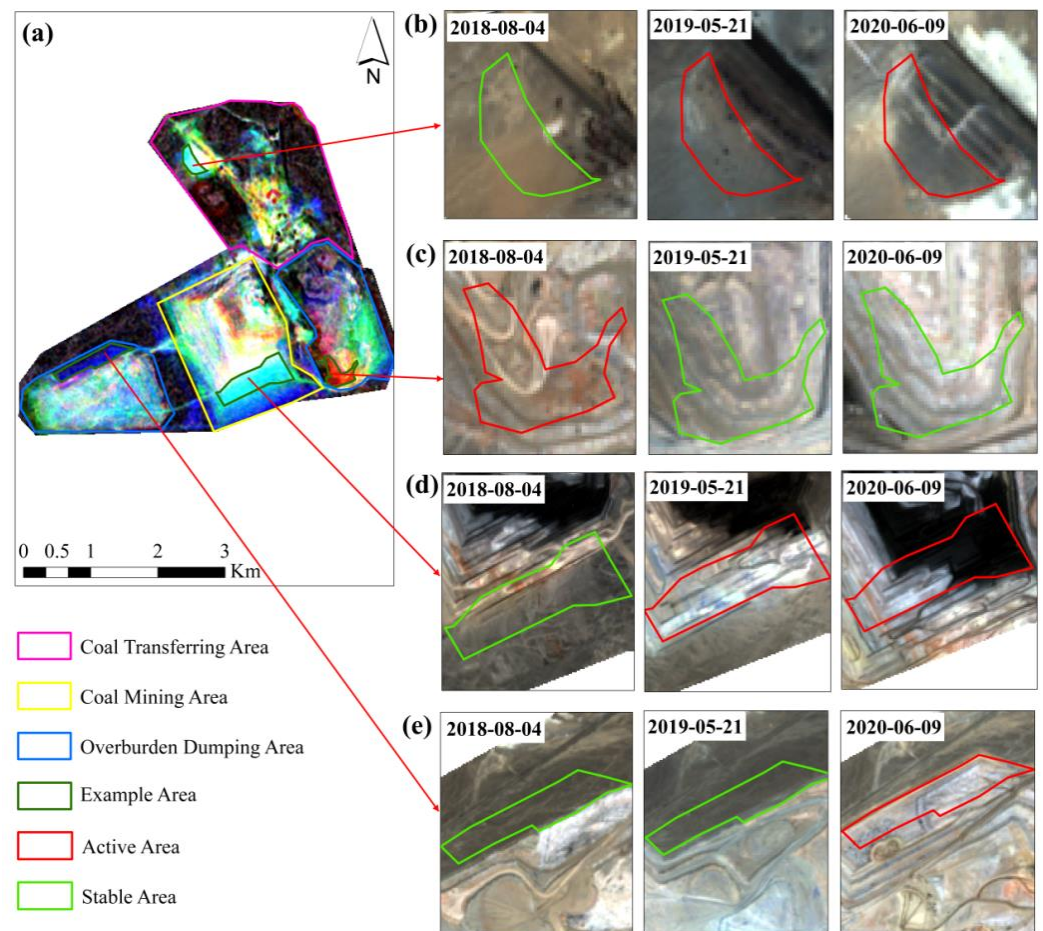


**Figure 8.** Interannual variation of mining activity maps in No. 1 open-pit coal mine: (a) The RGB composite map of the annually-averaged NDAI images, (b–e) Sentinel-2A MSI images which were captured on the 4 August 2018, 21 May 2019, and 9 June 2020, respectively. Four example areas from the coal mining area, two overburden dumping areas, and a coal transferring area are selected to validate the reliability of study results with the corresponding optical images.

#### 4.2.2. No. 2 Open-Pit Coal Mine

No. 2 open-pit coal mine includes two mining areas, one in the south and the second in the north. According to Figure 9a, the coal mining area and overburden dumping area of the first mining area show a color pattern (black) indicating no mining activity from 2018 to 2020. The coal transferring area also shows a color pattern (red) indicating that it has been active mainly in 2018. This suggests that although the coal mine has stopped mining, the coal pile in the coal transferring area has not been completely cleared. The same phenomenon is also seen in the optical images, where on 4 August 2018 there was still coal in the area, whereas on 21 May 2019 and 9 June 2020 the area was clear of coal (Figure 9b).



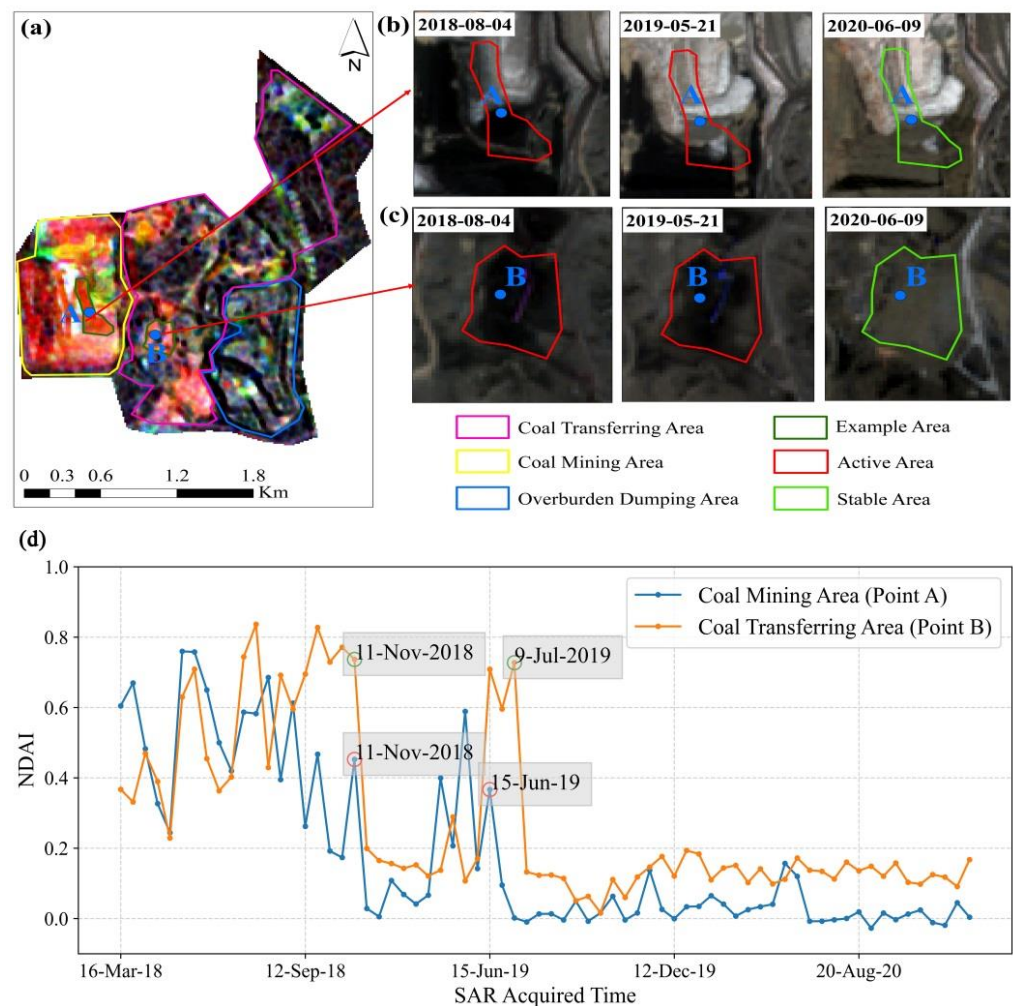


**Figure 10.** Interannual changes of mining activity maps over the second mining area of No. 2 open-pit coal mine: (a) The RGB composite map of the annually-averaged NDAI images; (b,c) Sentinel-2A MSI images which were captured 4 August 2018, 21 May 2019, and 9 June 2020, respectively. Two example areas from the coal mining and transferring areas are selected to validate the reliability of the using the optical images; (d) graph of the NDAI time-series with 12-day intervals for point A of the coal mining area and point B of the coal transferring area, showing specific date of surface activity.

Points A and B are also selected in the coal mining area and transferring area respectively, and the NDAI time series of these two points are plotted (Figure 10d). It is seen that the NDAI values for both the mining and transferring areas shifted between 0.2 and 0.8 before 11 November 2018, and reduced sharply to below 0.2 after 11 November. This indicates that the coal mine did not stop mining until November 2018. However, after a period of cessation, the NDAI value rose sharply again due to the ecological restoration after mining. The initial restoration was completed in July 2019 for the coal mining area and in June 2019 for the coal transferring area. This explains why coal was still present in the optical image on 21 May 2019. It is also clear in the optical images that the ground was covered with soil on 9 June 2020.

#### 4.2.3. No. 3 Open-Pit Coal Mine

The interannual variation of the mining activity map over the No. 3 open-pit coal mine is shown in Figure 11. It is seen in Figure 11a that there are large areas of white pixels distributed from south to north throughout the coal mining area. This indicates that the area has been always active from 2018 to 2020. In the southern half of the coal mining area,

the color patterns from pit floor to pit mouth are white (i.e., always active), cyan (i.e., active only in 2019 and 2020), and blue (i.e., active only in 2020). These indicate that this mine has been gradually being excavated southward from 2018 to 2020. According to Figure 11c,e, the process of pit floor and pit mouth moving southward shows that our experimental results are correct. In the northern half of the coal mining area, the pit benches that already existed before 2018 were also covered by white, cyan, and blue pixels, indicating that the area had undergone drastic changes over time. Intense activities at the pit bench are usually caused by the landfills. As shown in Figure 11b, the area was still a stable pit bench on 4 August 2018 and 21 May 2019; whereas, it had been landfilled with the overburden accumulated to the south on 9 June 2020. This is consistent with the results reported by the NDAI values. The overburden dumping area is dominated by black pixels that are always stable, and only a small part of the south side has an active color pattern. The above analysis results also show that our previous speculation is correct. The mine area mainly adopts the mining method of south digging and north filling.

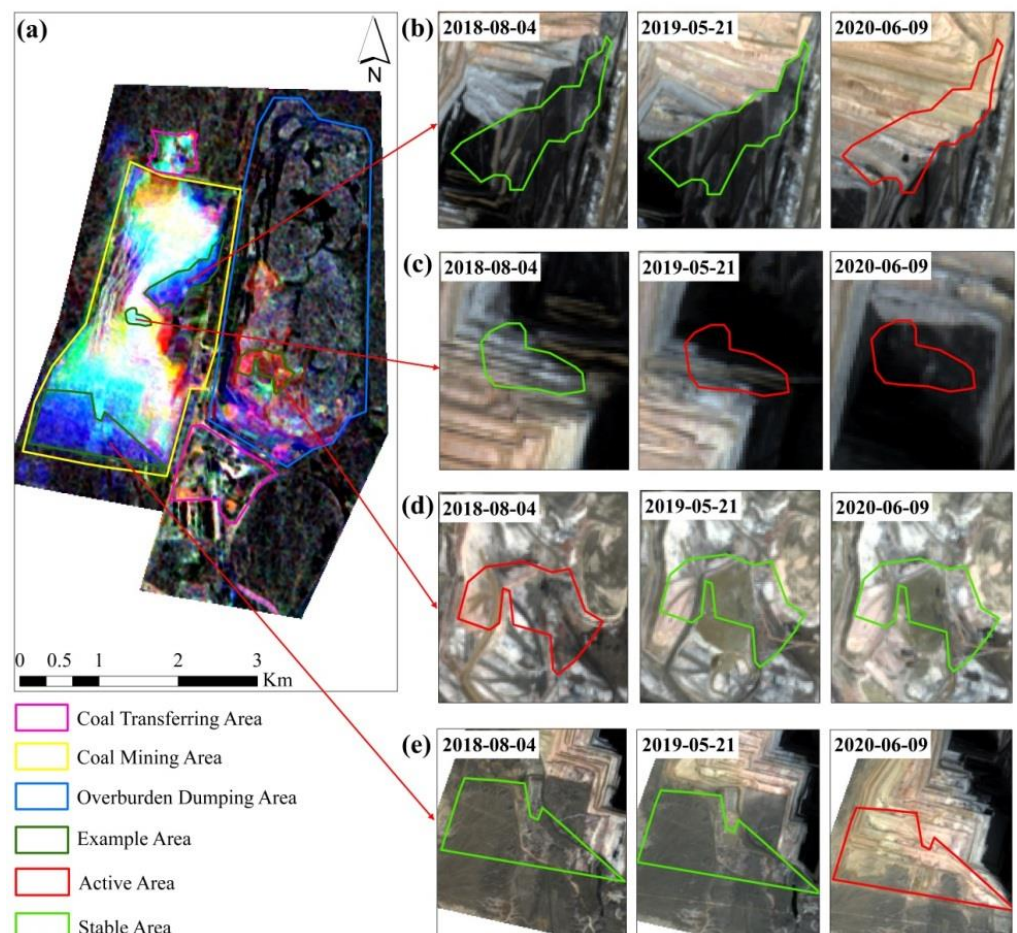


**Figure 11.** Interannual changes of mining activity maps over the No. 3 open-pit coal mine: (a) The RGB composite map of the annually-averaged NDAI images; (b–e) Sentinel-2A MSI images were captured on 4th of August 2018, 21st of May 2019 and 9th of June 2020, respectively. Four example areas from coal mining and overburden dumping areas are selected to validate the reliability of study results with corresponding optical images.

## 5. Discussion

To monitor the mining activities of the Wucaiwan open-pit mine from 2018 to 2020, normalized difference activity index (NDAI) based on coherence images is introduced to represent the changes in the mine areas. Compared with the coherence values that

emphasize surface stability, NDAI is used to represent the degree of surface activity, which is suitable for monitoring active mining areas.

In this study, the stable points acquired from the time-averaged and standard deviation of the coherence images are used to analyze and remove the decorrelation noise. The NDAI mainly relies on stable points that are effective at detecting temporal decorrelation to eliminate decorrelation noise in the target area. The decorrelation noise due to weather conditions such as rain and snow can be directly removed by excluding coherence images with spatially averaged coherence values of the stable points that are less than 0.9. This requires stable points which are close enough to the target region to have the same weather conditions. The NDAI as defined in Equation (3) is calculated to reduce the decorrelation noise caused by the spatial baselines as shown in Figure 6. Although the local topography-induced decorrelation is partly mitigated by averaging the coherence of the stable points distributed throughout the mine area, its corresponding induced errors are still present [51]. The distortion caused, in cases where the SAR look-angle is less than the back-slope slope of the terrain and is not illuminated by the radar beam, is referred to as the shadow [52]. Shadow area is shown in the SAR image as dark regions and has a high NDAI and can confuse active mining areas [53]. For example, the first mining area of the No. 2 open-pit coal mine stopped mining in November 2015, but still possesses several white color patterns that represent a consistently active status as shown in Figure 9a. We speculate that this is most likely due to the high-value NDAI caused by shadows. However, it is difficult for us to distinguish between the shadow area and the mining activity area in No. 1 and 3 open-pit coal mines that had been active. If the study area has both ascending and descending track data, we expect that combining them eliminates the shadow areas.

We used RGB composite technique to synthesize the annually-averaged NDAI to represent the interannual variation of mining activities. It is also possible to use quarterly or monthly data to represent feature changes. Furthermore, we only assign different meanings to red, green, blue, cyan, magenta, yellow, black, and white to indicate changes in the mine areas over time. However, RGB composite colors consist of more than just these eight colors and can potentially associate other meanings to other colors.

It is meaningful to analyze the NDAI time series for the mining areas that have ceased or are about to cease. Judging from the empirical values, if the NDAIs are consistently less than 0.2 in the mine areas, one can infer that the mining has ceased. For example, the second mine area of the No. 2 open-pit coal mine was stopped in 2017 due to the expiration of prospecting rights, but according to this study, the mine was still active in 2018. It however deems difficult to set a quantitative criterion to judge the state of the mine areas that had been active during the study period.

## 6. Conclusions

In this study, the mining status of four open-pit coal mines from the Wucaiwan coalfield in China was investigated using normalized difference activity index (NDAI) acquired based on InSAR coherence images. A total of 70 NDAI images were averaged to observe the overall mining activities between 2018 and 2020. The results show that No. 1 and 3 open-pit coal mines were more intensively active and produced more coal than No. 2. The RGB composite of annually-averaged NDAI images showed the interannual variation of mining activities. It was also found that the No. 1 and 3 open-pit coal mines had been continuously mined during the three years, while No. 2 open-pit coal mine was decommissioned as of 2018 due to the expiration of prospecting rights. Results were validated with corresponding Sentinel-2A optical images and related background information. Our results confirm the efficiency of the RGB composite scheme for monitoring time-series variation of the mine areas. The NDAI time-series graphs with 12 intervals were plotted for the No. 2 open-pit coal mine to observe its specific mining stoppage time. The graph for the first mining area indicates that the coal pile located in the coal transferring area was completely cleaned by April 2019. The graph for the second mining area indicates that the mine ceased operation in November 2018 and became rehabilitated in July 2019.

The monitoring results from four open-pit coal mines demonstrate the feasibility of using NDAI to monitor mining activity and the superiority of the RGB composite scheme to represent interannual variation in the mine areas. However, there are still some difficulties. Only Sentinel-1A ascending track data are available for this study area, and some parts of the mine pits may be obscured, hence actual information cannot be obtained due to the side-view imaging nature of SAR images. If both ascending and descending track data are made available, combining both to study the entire pit mining activities is suggested. Continuous monitoring of mining activity using high temporal resolution Sentinel-1A/B SAR imagery can save site measurement costs.

**Author Contributions:** Conceptualization, L.W.; methodology, L.W.; software, L.W.; validation, L.W. and X.S.; formal analysis, L.W.; data curation, L.W.; writing—original draft preparation, L.W.; writing—review and editing, L.W. and B.C.; visualization, L.W. and B.C.; supervision, L.Y. and W.W.; project administration, L.Y.; funding acquisition, L.Y. and W.W. All authors have read and agreed to the published version of the manuscript.

**Funding:** This research was supported by the Strategic Priority Research Program of Chinese Academy of Sciences (Grant No. XDA20020101).

**Data Availability Statement:** The data presented in this study are available on request from the corresponding author.

**Acknowledgments:** We thank the journal’s editors and reviewers for their kind comments and valuable suggestions to improve the quality of this paper.

**Conflicts of Interest:** The authors declare no conflict of interest.

## References

1. Yudovich, Y.E.; Ketris, M.P. Mercury in coal: A review Part 2. Coal use and environmental problems. *Int. J. Coal Geol.* **2005**, *62*, 135–165. [[CrossRef](#)]
2. Ren, X.; Wang, H.; Liu, Y.; Zheng, J. Suitability of habitat distribution change analysis of Kalamaili Mountain Ungulate Nature Reserve. *Xinjiang Agric. Sci.* **2016**, *53*, 553–562.
3. Liu, X. Evaluation of Environmental Quality Based on GIS—Take Wucaiwan Coal Mine in Xinjiang as an Example. Master’s Thesis, China University of Geosciences, Beijing, China, 2018.
4. Ananda, I.; Aswari, F.; Narmaningrum, D.; Nugraha, A.; Asidiqi, M.; Setiawan, Y. Modeling of erosion on Jelateng watershed using USLE method, associated with an illegal mining activities (PETI). In *IOP Conference Series: Earth and Environmental Science, Proceedings of the 2nd International Conference of Indonesian Society for Remote Sensing (ICOIRS), Yogyakarta, Indonesia, 17–20 October 2016*; IOP Publishing: Bristol, UK, 2016; Volume 47, p. 012025.
5. Tong, X.; Liu, X.; Chen, P.; Liu, S.; Luan, K.; Li, L.; Liu, S.; Liu, X.; Xie, H.; Jin, Y.J.R.S. Integration of UAV-based photogrammetry and terrestrial laser scanning for the three-dimensional mapping and monitoring of open-pit mine areas. *Remote Sens.* **2015**, *7*, 6635–6662. [[CrossRef](#)]
6. Chen, J.; Li, K.; Chang, K.-J.; Sofia, G.; Tarolli, P. Open-pit mining geomorphic feature characterisation. *Int. J. Appl. Earth Obs. Geoinf.* **2015**, *42*, 76–86. [[CrossRef](#)]
7. Gong, C.; Lei, S.; Bian, Z.; Liu, Y.; Zhang, Z.; Cheng, W.J.R.S. Analysis of the development of an erosion gully in an open-pit coal mine dump during a winter freeze-thaw cycle by using low-cost UAVs. *Remote Sens.* **2019**, *11*, 1356. [[CrossRef](#)]
8. Nascimento, F.S.; Gastauer, M.; Souza-Filho, P.W.M.; Nascimento, W.R.; Santos, D.C.; Costa, M.F.J.R.S. Land cover changes in open-cast mining complexes based on high-resolution remote sensing data. *Remote Sens.* **2020**, *12*, 611. [[CrossRef](#)]
9. Asner, G.P.; Tupayachi, R. Accelerated losses of protected forests from gold mining in the Peruvian Amazon. *Environ. Res. Lett.* **2017**, *12*, 094004. [[CrossRef](#)]
10. Wu, Q.; Song, C.; Liu, K.; Ke, L. Integration of TanDEM-X and SRTM DEMs and spectral imagery to improve the large-scale detection of open-cast mining areas. *Remote Sens.* **2020**, *12*, 1451. [[CrossRef](#)]
11. Fernández-Lozano, J.; González-Díez, A.; Gutiérrez-Alonso, G.; Carrasco, R.M.; Pedraza, J.; García-Talegón, J.; Alonso-Gavilán, G.; Remondo, J.; Bonachea, J.; Morellón, M. New Perspectives for UAV-Based Modelling the Roman Gold Mining Infrastructure in NW Spain. *Minerals* **2018**, *8*, 518. [[CrossRef](#)]
12. Massonnet, D.; Feigl, K.L. Radar interferometry and its application to changes in the Earth’s surface. *Rev. Geophys.* **1998**, *36*, 441–500. [[CrossRef](#)]
13. Lu, Z. InSAR imaging of volcanic deformation over cloud-prone areas—Aleutian islands. *Photogramm. Eng. Remote Sens.* **2007**, *73*, 245–257. [[CrossRef](#)]
14. Novellino, A.; Bateson, L.; Jordan, C. Ground motion baseline analysis of the cheshire uk geoenergy observatory. *Sci. Rep.* **2021**, *11*, 15684. [[CrossRef](#)]

15. Sun, Q.; Zhang, L.; Ding, X.; Hu, J.; Li, Z.; Zhu, J. Slope deformation prior to Zhouqu, China landslide from InSAR time series analysis. *Remote Sens. Environ.* **2015**, *156*, 45–57. [[CrossRef](#)]
16. Li, Z.; Zhou, J.; Tian, B. The glacier movement estimation and analysis with InSAR in the Qinghai-Tibetan plateau. In Proceedings of the 2009 IEEE International Geoscience and Remote Sensing Symposium, Cape Town, South Africa, 12–17 July 2009; pp. II-578–II-581.
17. Chaussard, E.; Wdowinski, S.; Cabral-Cano, E.; Amelung, F. Land subsidence in central Mexico detected by ALOS InSAR time-series. *Remote Sens. Environ.* **2014**, *140*, 94–106. [[CrossRef](#)]
18. Ng, A.H.-M.; Ge, L.; Zhang, K.; Chang, H.-C.; Li, X.; Rizos, C.; Omura, M. Deformation mapping in three dimensions for underground mining using InSAR—Southern highland coalfield in New South Wales, Australia. *Int. J. Remote Sens.* **2011**, *32*, 7227–7256. [[CrossRef](#)]
19. Paradella, W.R.; Ferretti, A.; Mura, J.C.; Colombo, D.; Gama, F.F.; Tamburini, A.; Santos, A.R.; Novali, F.; Galo, M.; Camargo, P.O.; et al. Mapping surface deformation in open pit iron mines of Carajás Province (Amazon Region) using an integrated SAR analysis. *Eng. Geol.* **2015**, *193*, 61–78. [[CrossRef](#)]
20. Hartwig, M.E.; Paradella, W.R.; Mura, J.C. Detection and monitoring of surface motions in active open pit Iron mine in the Amazon region, using persistent scatterer interferometry with TerraSAR-X satellite data. *Remote Sens.* **2013**, *5*, 4719–4734. [[CrossRef](#)]
21. Wang, S.; Lu, X.; Chen, Z.; Zhang, G.; Ma, T.; Jia, P.; Li, B. Evaluating the Feasibility of illegal open-pit mining identification using insar coherence. *Remote Sens.* **2020**, *12*, 367. [[CrossRef](#)]
22. Chaussard, E.; Kerosky, S. Characterization of Black Sand Mining Activities and Their Environmental Impacts in the Philippines Using Remote Sensing. *Remote Sens.* **2016**, *8*, 100. [[CrossRef](#)]
23. Chatterjee, R.; Lakhera, R.; Dadhwal, V. InSAR coherence and phase information for mapping environmental indicators of opencast coal mining: A case study in Jharia Coalfield, Jharkhand, India. *Can. J. Remote Sens.* **2010**, *36*, 361–373. [[CrossRef](#)]
24. Zhang, J. Insar Collaborative Monitoring Mode and Multi-Mode Computing Services for Geohazards Identification in Open-Pit Mining Area. *ISPRS-Int. Arch. Photogramm. Remote Sens. Spat. Inf. Sci.* **2021**, *43*, 241–247. [[CrossRef](#)]
25. Beijing Huaxia Mountain Ecological Environment Technology Co., Ltd. *Water and Soil Conservation Plan Report of No.1 Open-Pit Coal Mine and Coal Preparation Plant (Phase I) in Wucaiwan Mining Area of Xinjiang Yihua Mining Co., LTD*; Ministry of Water Resources of the People’s Republic of China: Beijing, China, 2018.
26. Xinjiang Coal Design and Research Institute Co., Ltd. *Wucaiwan Mine Area No. 2 Open-Pit Coal Mine Phase I Project Eia Report in Xinjiang Tianlong Hope Energy Co., LTD*; Morning News in Xinjiang Uygur Autonomous Region: Xinjiang, China, 2018.
27. Inner Mongolia Coal Mine Design Research Institute Co. Ltd. *Feasibility Study Report of No.3 Open-Pit Coal Mine in Wucaiwan Mining Area, Zhundong Coalfield, Xinjiang*; Inner Mongolia Autonomous Region Engineering Consulting Association: Inner Mongolia, China, 2019.
28. Xu, X. Analysis of Spatial-Temporal Changes of Desert Vegetation and Causes in Wucaiwan Open-Pit Mining Area. Master’s Thesis, Henan Polytechnic University, Jiaozuo, China, 2020.
29. Zhang, Y. Evaluation on Ecological Security of Wucaiwan Opencast Mine in Xinjiang. Master’s Thesis, Xinjiang University, Xinjiang, China, 2014.
30. Zan, F.D.; Guarnieri, A.M. TOPSAR: Terrain Observation by Progressive Scans. *IEEE Trans. Geosci. Remote Sens.* **2006**, *44*, 2352–2360. [[CrossRef](#)]
31. Farkas, P.; Hevér, R.; Greneczy, G. Geodetic integration of Sentinel-1A IW data using PSInSAR in Hungary. In Proceedings of the EGU General Assembly Conference Abstracts, Vienna, Austria, 12–17 April 2015; p. 13483.
32. Torres, R.; Snoeij, P.; Davidson, M.; Bibby, D.; Lokas, S. The Sentinel-1 mission and its application capabilities. In Proceedings of the 2012 IEEE International Geoscience and Remote Sensing Symposium, Munich, Germany, 22–27 July 2012; pp. 1703–1706.
33. Alaska Satellite Facility (ASF). Available online: <https://www.asf.alaska.edu/> (accessed on 6 May 2021).
34. Novellino, A.; Brown, T.J.; Bide, T.; Thúc Anh, N.T.; Petavratzi, E.; Kresse, C. Using Satellite Data to Analyse Raw Material Consumption in Hanoi, Vietnam. *Remote Sens.* **2021**, *13*, 334. [[CrossRef](#)]
35. Kumar, P.; Sajjad, H.; Tripathy, B.R.; Ahmed, R.; Mandal, V.P. Prediction of spatial soil organic carbon distribution using Sentinel-2A and field inventory data in Sariska Tiger Reserve. *Nat. Hazards* **2018**, *90*, 693–704. [[CrossRef](#)]
36. Copernicus Data Center (CDC). Available online: <https://scihub.copernicus.eu/> (accessed on 6 May 2021).
37. Tang, W.; Motagh, M.; Zhan, W. Monitoring active open-pit mine stability in the Rhenish coalfields of Germany using a coherence-based SBAS method. *Int. J. Appl. Earth Obs. Geoinf.* **2020**, *93*, 102217. [[CrossRef](#)]
38. United States Geological Survey (USGS). Available online: <https://earthexplorer.usgs.gov/> (accessed on 31 May 2021).
39. Derauw, D. Phase unwrapping using coherence measurements. In Proceedings of the Synthetic Aperture Radar and Passive Microwave Sensing, Paris, France, 25–28 September 1995; pp. 319–324.
40. Seymour, M.; Cumming, I. Maximum likelihood estimation for SAR interferometry. In Proceedings of the IGARSS’94-1994 IEEE International Geoscience and Remote Sensing Symposium, Pasadena, CA, USA, 8–12 August 1994; pp. 2272–2275.
41. Bouaraba, A. Coherent change detection using high resolution SAR images. Ph.D. Thesis, Ecole Militaire Polytechnique/Ecole Royale Militaire, Paris, France, 2014.
42. SNAP. Available online: <https://step.esa.int/main/toolboxes/snap/> (accessed on 2 June 2021).

43. Ferretti, A.; Monti-Guarnieri, A.; Prati, C.; Rocca, F.; Massonet, D. *InSAR Principles-Guidelines for SAR Interferometry Processing and Interpretation*; ESA Publication: Noordwijk, The Netherlands, 2007.
44. Hanssen, R.F. *Radar Interferometry: Data Interpretation and Error Analysis*; Springer Science & Business Media: New York, NY, USA, 2001; Volume 2.
45. Hoen, E.W.; Zebker, H.A. Penetration depths inferred from interferometric volume decorrelation observed over the Greenland ice sheet. *Trans. Geosci. Remote Sens.* **2000**, *38*, 2571–2583.
46. Zebker, H.A.; Villasenor, J. Decorrelation in interferometric radar echoes. *IEEE Trans. Geosci. Remote Sens.* **1992**, *30*, 950–959. [[CrossRef](#)]
47. Lee, H.; Liu, J.G. Analysis of topographic decorrelation in SAR interferometry using ratio coherence imagery. *Trans. Geosci. Ang Remote Sens.* **2001**, *39*, 223–232.
48. Yagüe-Martínez, N.; Prats-Iraola, P.; Gonzalez, F.R.; Brcic, R.; Shau, R.; Geudtner, D.; Eineder, M.; Bamler, R. Interferometric processing of Sentinel-1 TOPS data. *IEEE Trans. Geosci. Remote Sens.* **2016**, *54*, 2220–2234. [[CrossRef](#)]
49. Rosen, P.A.; Hensley, S.; Joughin, I.R.; Li, F.K.; Madsen, S.N.; Rodriguez, E.; Goldstein, R.M. Synthetic aperture radar interferometry. *Proc. IEEE* **2000**, *88*, 333–382. [[CrossRef](#)]
50. Jung, J.; Kim, D.-J.; Lavallo, M.; Yun, S.-H. Coherent change detection using InSAR temporal decorrelation model: A case study for volcanic ash detection. *Trans. Geosci. Remote Sens.* **2016**, *54*, 5765–5775. [[CrossRef](#)]
51. Moon, J.; Lee, H. Analysis of Activity in an Open-Pit Mine by Using InSAR Coherence-Based Normalized Difference Activity Index. *Remote Sens.* **2021**, *13*, 1861. [[CrossRef](#)]
52. Moreira, A.; Prats-Iraola, P.; Younis, M.; Krieger, G.; Hajnsek, I.; Papathanassiou, K.P. A tutorial on synthetic aperture radar. *IEEE Geosci. Remote Sens. Mag.* **2013**, *1*, 6–43. [[CrossRef](#)]
53. Moon, J.; Kim, G.; Lee, H. Surface Change Detection in the March 5Youth Mine Using Sentinel-1 Interferometric SAR Coherence Imagery. *Korean J. Remote Sens.* **2021**, *37*, 531–542.